

Flash-induced defects in single-crystal 8YSZ characterized by TEM, XRD, and Raman spectroscopy

Seohyeon Jo¹  | Moritz Kindelmann^{2,4,5}  | Dylan Jennings^{2,4} | Luca Balice² |
 Yoo Jung Sohn²  | Walter Sebastian Scheld²  | Martin Bram² |
 Olivier Guillon^{2,3}  | Joachim Mayer^{4,5} | Rishi Raj^{1,6} 

¹Materials Science and Engineering Program, University of Colorado Boulder, Boulder, Colorado, USA

²Institute of Energy and Climate Research, Materials Synthesis and Processing (IEK-1), Forschungszentrum Jülich GmbH, Jülich, Germany

³JARA-Energy, JüJAR Aachen Research Alliance, Jülich, Germany

⁴Ernst-Ruska Centre for Microscopy and Spectroscopy with Electrons (ER-C), Forschungszentrum Jülich, Jülich, Germany

⁵RWTH Aachen University, Central Facility for Electron Microscopy (GFE), Aachen, Germany

⁶Department of Mechanical Engineering, University of Colorado Boulder, Boulder, Colorado, USA

Correspondence

Seohyeon Jo, Materials Science and Engineering Program, University of Colorado Boulder, Boulder, CO, USA.
 Email: seohyeon.jo@colorado.edu

Funding information

Office of Naval Research, Grant/Award Number: N00014-18-1-2270; Deutsche Forschungsgemeinschaft, Grant/Award Numbers: MA 1280/69-1, Rh 146/1, SPP 1959

Abstract

We present direct evidence, for the first time, for the flash-induced generation of crystal defects in single-crystal cubic zirconia. The defects are characterized by multiple techniques. The crystals were flashed and then cooled down to ambient temperature in Ar atmosphere to preserve the electronic conductivity from the steady state of flash. Transmission electron microscopy revealed colonies of defects. The crystal structure, the non-stoichiometry, and the electronic structure of oxygen ions within these colonies were characterized. They consist of oxygen-depleted compositions. Selected area electron diffraction revealed the structure of these zirconia suboxides to be epitaxially coherent with the parent cubic structure but with a smaller lattice parameter. Electron energy loss spectroscopy spectra showed the peak near 25 mV to shift toward metallic zirconium. The electronic conductivity of the flashed cubic zirconia is attributed to this suboxide phase. The phase also gave rise to new peaks in Raman spectroscopy. A surprising finding was the presence of a distinct, ~30 nm thick layer of the suboxide on the surface of the crystal. The surface layer showed a high degree of oxygen deficiency. It was also epitaxial, but with an even smaller lattice parameter than the defect colonies underneath the surface. Mechanical polishing of the crystal to remove this surface layer gave a broad view of the interconnected network of defects across the entire specimen; the length scale of this network was about 0.2 mm. Recent work, where an overlay of a magnetic field caused the flash to migrate from a flashing surface into a free-standing workpiece, suggests the presence of evanescent plasma, which may have a connection to this surface layer.

KEY WORDS

defects, flash sintering, microstructure, transmission electron microscopy, zirconia, zirconium suboxide

1 | INTRODUCTION

Electric current-assisted sintering is mentioned in patents dating a century ago. More recently, microwave sintering^{1,2} and spark plasma sintering (SPS) have spear-headed a new era of field-assisted sintering. Commercial availability of SPS systems^{3,4} has spurred practical applications, especially in instances where SPS is an enabling technology for consolidating those metals and ceramics that are nominally difficult to densify.^{5,6}

The latest development has been the discovery of “flash sintering,” where dog bone-shaped powder-pressed samples are sintered below 1000°C by applying field and current *directly* to the specimen.⁷ The experiment is carried out with open access to the workpiece, which enables in-operando measurements of the temperature with a pyrometer, electroluminescence with a spectrometer, and sintering strain with a camera. The simplicity of the experiment has led to *in situ* X-ray synchrotron experiments where the temperature has been measured with a platinum standard⁸; they have also shown the time-dependent emergence of new, far-from-equilibrium phases.⁹ Unusual lattice expansion, far greater than thermal expansion, has been reported¹⁰ to have been measured in synchrotron experiments.

Flash sintering has been shown to apply widely¹¹ to oxide ceramics,^{12–21} non-oxide ceramics,^{22–27} and, most recently, to metals.²⁸ The flash effect is seen in single crystals as well, which suggests that it is a bulk and not a grain boundary phenomenon. An overview of developments since 2010 is given in review papers.^{11,29,30}

The mechanism(s) of the flash phenomena remain controversial. The sudden increase in conductivity at the onset of flash, an ever-present feature of flash, has led to suggestions that flash results from Joule heating.^{30–33} Other suggestions include defect generation,^{7,34–41} local heating at grain boundaries,^{42–46} and electrochemical reactions.^{47,48} In particular, the creation of oxygen vacancies and consequent blackening of the oxide under flash conditions have been experimentally assessed and explained phenomenologically.^{49–52}

Nevertheless, the evidence for defect generation continues to grow:

- (i) Lebrun et al. have reported a residual lattice expansion in yttria-stabilized zirconia (YSZ), which was measured during *in situ* X-ray experiments at synchrotrons.⁹ Ab initio calculations, carried out in parallel, explained the lattice expansion by Frenkel pairs of Zr and O ions.⁹
- (ii) Kathiria et al.⁴⁰ showed that flash leads to weakening of the elastic modulus in YSZ, which was confirmed

by molecular dynamics (MD) simulations of softening induced by Frenkel pairs.

- (iii) Earlier, MD simulations by Jongmann et al.^{39,40,53} have shown that Frenkel defects are generated by injecting phonons at the edge of the Brillouin zone, above the Debye temperature.

Calorimetric experiments where flash is carried out by increasing the current at a constant rate (so-called current-rate experiments) have consistently shown the presence of an endothermic reaction, whereby the input electrical energy is always greater than the energy dissipated by radiation, convection, and in specific heat.⁵⁴ Translating this energy deficit into the concentration of Frenkel pairs yields very large numbers, many orders of magnitude greater than the values expected from thermal equilibrium. This colossal generation of defects suggests that flash is a nonequilibrium phenomenon.

The flash phenomenon in ceramics is described in three stages.⁵⁵ The first, Stage I, is an incubation stage. Next, there is an abrupt increase in conductivity (also accompanied by superlative rates of sintering), which is known as Stage II. The rise in conductivity is controlled by switching the power supply from voltage to current control; this, Stage III, is a “steady state” of flash held under constant current. The transition to high conductivity is accompanied by bright electroluminescence,⁵⁶ which *persists even if the furnace is turned off*. Indeed, samples continue to luminesce even when immersed in liquid nitrogen. Quenching in LN₂ preserves the state of high conductivity at ambient temperature, which is electronic in nature.⁵⁷

Specimens that are nominally cooled down in ambient atmosphere often revert to their insulating state.^{58,59} Therefore, the in-flash immersion and LN₂-quenched samples⁵⁷ offer an opportunity to study the state of the structure and defects that would have existed in the flash state.

The transition to high conductivity at the advent of Stage II also spells a transition from ionic to electronic conductivity in YSZ. This result has been confirmed by *in situ* impedance spectroscopy,⁶⁰ as well as by the metallic nature of the LN₂ quenched samples of YSZ.⁵⁷ Phenomenological evidence suggests that the transition to electronic conductivity is a general characteristic of flash, even in insulators such as yttria and strontium titanate.

The electronically conducting state (in cubic zirconia) can also be preserved if flash is carried out in Ar atmosphere and then cooled down to ambient temperature, within the Ar environment.^{58,59} In this article, we characterize the defect structure in these single crystal specimens by transmission electron microscopy (TEM), EELS, X-ray, and Raman. We find the presence of large colonies

of defects that form their own phase, albeit epitaxially coherent with the parent cubic crystal. This new phase is highly deficient in oxygen—we call it a suboxide of zirconia.

There have been TEM studies of defects generated during flash. Wang et al.⁶¹ found dislocations and stacking faults in flash-sintered (polycrystalline) titania. They have also shown⁶² dislocations in 3 mol% YSZ and the precipitation of yttrium at the grain boundaries. The dislocations and stacking faults are observed near the anode but not at the cathode, suggesting a relationship with the oxygen vacancies.

Defect structures in strontium titanate have been reported. Evolution of the non-stoichiometric Ruddlesden-Popper phase of higher conductivity was seen by Karakuscu et al.¹⁵ A gradient in the point defects in flash-sintered undoped strontium titanate and iron-doped strontium titanate has been observed by Rheinheimer et al.⁶³ They observed the Ti-rich phase in the undoped sample and iron segregation in doped sample at the positive electrode. In situ TEM results with ZnO were reported by Schwarzbach et al.⁶⁴ They observed sintering, migrating grain boundaries, and changes in conductivity, but did not find the presence of a conductive second phase.

In this article, we present an exhaustive characterization of electronically conducting single crystals of cubic zirconia that were flashed and then nominally cooled in Ar atmosphere. The TEM studies included imaging, selected area electron diffraction (SAED), and electron energy loss spectroscopy (EELS). Large, interconnected colonies of defects that were highly oxygen-deficient were seen. These colonies formed a hetero-epitaxial, coherent phase within the parent single crystal. This phase had a smaller lattice parameter than the parent crystal. TEM also revealed an even more severely oxygen-deficient surface layer, which remained epitaxially coherent with the cubic structure of the parent crystal.

2 | EXPERIMENTAL METHODS

2.1 | Single-crystal yttria-stabilized cubic zirconia specimens made by flash in Ar atmosphere

Single-sided polished yttria-stabilized cubic zirconia (8YSZ) single crystals, with surfaces having a (1 0 0) orientation, were obtained from MSE Supplies. The single crystal was cut into 5 mm long × 2 mm wide × 1 mm thick rectangular shapes, as seen in Figure 1A. The single crystal was cut using a precision saw (TechCut 4, Allied)

with diamond wafering blades (Buehler). One side was polished to obtain a smooth, mirrorlike surface.

For the flash experiment, ~1 mm of each end was wrapped with platinum wires. Pt paste was applied to achieve good electrical contact between the electrodes and the single crystal.

The single crystal was flashed within a glove box with Ar atmosphere. The oxygen partial pressure was 20–100 ppm. The DC power supply (Series KL, Glassman High Voltage, Inc.) was used to initiate the flash and control the electrical parameters. The electrical parameters used in the flash of the single crystal are given in Figure 1B.

We used the constant current rate mode to avoid the possible thermal shock at the flash onset, which can occur by a sudden increase in current at the onset of flash in voltage-to-current experiments. Flash was initiated at a furnace temperature of 800°C, with a field of 25 V cm⁻¹, with the current limit set to 150 mA mm⁻². (The second peak, a nonlinearity in the electric field curve in Figure 1B, likely arose from an imperfect contact.) Upon reaching this current limit, the specimen was moved out of the furnace into the Ar ambient environment within the glove box. Next, the current was increased in steps of 50 mA mm⁻² min⁻¹ up to 150, 300, and 600 mA mm⁻², in different specimens, thereby yielding three specimens which are called Ar150, Ar300, and Ar600. In each instance, the maximum current was held for 1 min before it was turned off. Specimens with different current limits would help to assess the influence of current density on the defect structure.

The above procedure (moving the specimens out into the ambient temperature—within the glove box) was necessary to avoid thermal shock because high currents imposed at the first onset of flash, within the furnace, would sometimes cause the specimen to splinter.

2.2 | Measurement of electrical conductivity

The DC electrical conductivity of the flashed specimens was measured at room temperature in ambient atmosphere. I-V curves were obtained with ARBIN BT2043. The electronic conductivity was further confirmed by impedance spectroscopy (HP 4192A) for several specimens (please refer to Figure S1). The DC conductivity parallel to the direction of the field applied during flash, and then in the perpendicular direction, were measured. To eliminate the effect of a surface layer on the conductivity (see TEM results in the following section for a description of the surface layer), about 50 µm of the surface layer was removed by mechanical polishing, and the conductivity was measured again.

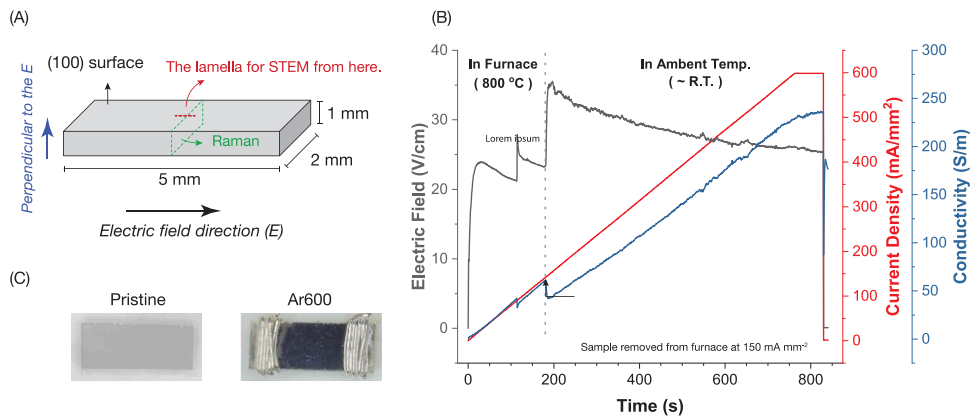


FIGURE 1 (A) Specimen geometry. (B) Flash curves of Ar600. Flash was initiated at a furnace temperature of 800°C by increasing the current at a constant rate. Once the current reached 150 mA mm⁻², the specimens were moved into the ambient temperature (within the glove box) while maintaining the flash state. Thereafter the current was increased stepwise to produce three different specimens flashed up to different current densities. (C) The image of the pristine and the Ar600 specimen. The wires at each end of Ar600 is Pt wires.

In-operando conductivities measured while the specimens were held in the steady state of flash (Stage III) are reported in reference⁵⁸; they have been shown to increase with the flash current, presumably because the specimen temperature rises with current.

2.3 | Characterization of defects

The specimens were characterized by TEM, XRD, and Raman spectroscopy. Specimens for TEM were cut parallel to the (1 0 0) surface by focused ion beam (FEI Helios NanoLab 400S FIB-SEM), as shown in Figure 1A. The lamella was taken out from the middle of the specimen's surface in such a way that the surface edge, seen in the TEM, was parallel to the electric field.

TEM analysis was carried out in the following ways:

- (i) Energy-dispersive X-ray spectroscopy (Hitachi HF5000, FEI Titan G2 80-200 ChemiSTEM). Line scans for EDS were done with a standardless (Cliff-Lorimer) method. EELS—see below—and some EDS analyses were done with “hyperspy.”⁶⁵
- (ii) Low-loss EELS (Hitachi HF5000).
- (iii) Core-loss EELS (FEI Titan G2 80-200 ChemiSTEM) and,
- (iv) SAED (FEI Titan Tecnai G2 F20).
- (v) ChemiSTEM: high angle annular dark field (HAADF) images were obtained with Hitachi HF5000, FEI Titan G2 80-200.

X-ray Diffraction were conducted using the X-ray powder diffractometer, Empyrean (Malvern Panalytical, Almelo, Netherlands). The mirror-polished surface of flashed and un-flashed single crystals were

scanned with two-theta values of 20 to 140° in steps of 0.013°.

Raman spectroscopy mapping (in Via Qontor, Renishaw) was performed in the middle of the cross-section of Ar600, as shown in Figure 1A. A 532 nm laser (~2.5 mW) was used with a grating of 2400 l mm⁻¹ and a measuring time of 1 s per spectrum. The spectra were collected with a step size of $(x, y) = (1 \mu\text{m}, 1 \mu\text{m})$ over an $80 \mu\text{m} \times 40 \mu\text{m}$ area, resulting in a total number of 3321 spectra. The spectra were processed, including cosmic ray removal and normalization. The final mappings were averaged into a single spectrum.

3 | RESULTS

3.1 | Electronic conductivity

The conductivities were measured at room temperature—in air—of specimens cooled down from flash in Ar atmosphere. Three specimens, Ar150, Ar300, and Ar600, were measured.

The entire cross-section of all specimens was black, implying electronic conductivity, consistent with the results from in-flash immersion and quenching in liquid nitrogen.⁵⁷ The Hall effect measurement confirmed n-type electronic conductivity.⁵⁹

Conductivities of the three specimens are shown in Figure 2A. The conductivity increases very significantly with the current limit used in flash. Additionally, in Figure 2B, the conductivity measured along the direction of the electric current is significantly higher than normal.

As shown later, the conductivity of the specimens degraded considerably when the surface layer was

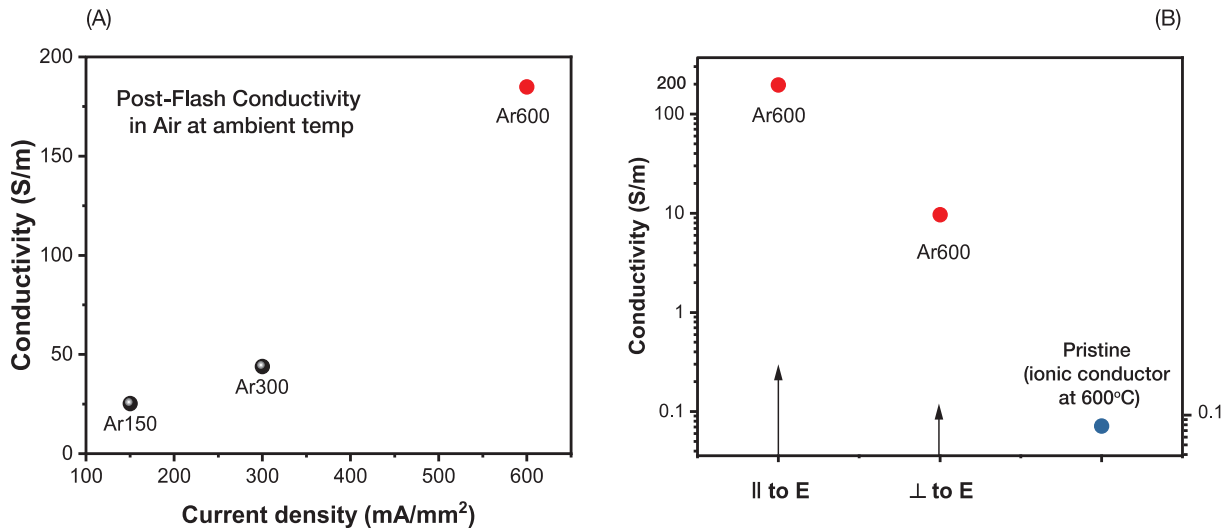


FIGURE 2 (A) Conductivities of specimens flashed up to different current densities. (B) Conductivity of Ar600 measured parallel and perpendicular to the applied field, at ambient temperature after flash. The ionic conductivity of the as-received sample was measured at 600°C, since it is insulating at room temperature.

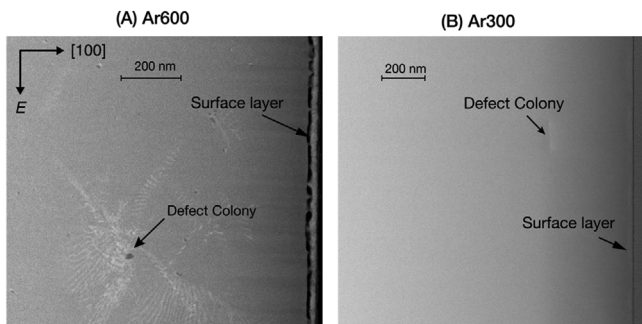


FIGURE 3 Overview images obtained by transmission electron microscopy for Ar600 and Ar300. The bright areas are evidence of defect colonies. The higher intensity in Ar600 suggests higher defect concentrations than in Ar300. The dendritic growth of the colony in Ar600 is noteworthy; it suggests that the formation of the colonies is a nucleation and growth process. The surface layer is discussed later in this article in Section 3.4.

removed by surface polishing. These results are discussed in Section 3.4.

3.2 | Transmission electron microscopy

The HAADF images from Ar600 and Ar300 samples are shown in Figure 3. The brighter regions were seen throughout the flashed samples. They were “brighter” in Ar600 than in Ar300. These regions are being called “defect colonies.” We shall infer that these colonies are responsible for the electronic conductivity.

The samples show the presence of a 30 nm thick surface layer in the Ar600 specimen, seen on the right side in Figure 3A. The edge of the surface layer is parallel to

the direction of the flash current. In the case of Ar300, the defect colonies are concentrated near the surface but do not form a continuous layer. A comparison between Ar600 and Ar300 reflects a connection between flash current and defect generation: The defect colonies are more intense in Ar600.

3.2.1 | Characterization of the crystal interior below the surface layer (Ar600)

The EDS scans of crystal interior are shown in Figure 4. The bright area in Figure 4A consists of defect colonies. The line scan in Figure 4B shows the defect colony to be significantly non-stoichiometric with a higher Zr/O ratio. The EDS mapping of the elements given in Figure 4C is consistent with low O and high Zr within the defect colonies.

It is possible to analyze the composition of the crystal matrix outside the defect colonies from the atom ratios of Zr:Y:O as measured on the extreme right edge of the line scan in Figure 4B. They yield approximately Zr:Y:O::(32):(4):(64). Ideally, in 8YSZ, it is expected that the relative atom percent should be Zr:Y:O::(29.2):(5.1):(65.6). The change in the zirconium atom fraction is significantly greater than the error range of Zr, which is expected to be less than 0.2 wt%.⁶⁶ It is, therefore, inferred that the zirconia is oxygen deficient even within the crystal matrix lying outside the defect colonies, which is consistent with the uniform black appearance of the single crystal after flash.

EELS spectra obtained within and just adjacent to the defect colonies are shown in Figure 5. The defect colony

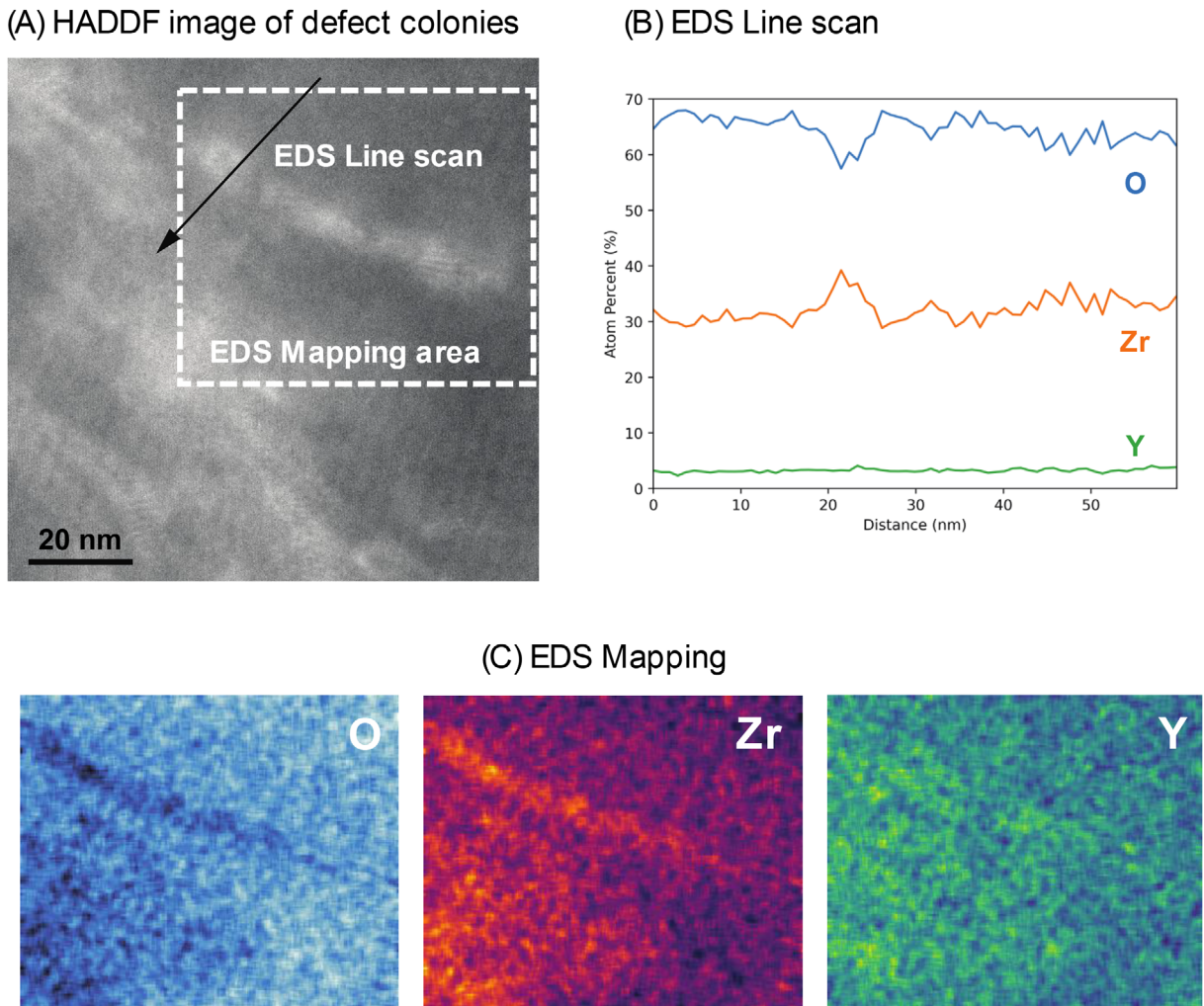


FIGURE 4 (A) & (B) A line scan across a defect colony showing deficit of O atoms. (C) EDS maps confirming oxygen deficit and correspondingly apparent enrichment of Zr.

seen in Figure 5A corresponds to the one seen in the HAADF image in Figure 4A.

The data for core-loss and low-loss EELSSs are given in Figure 5B. The former is obtained at the ~530 eV oxygen edge, and the latter in the 0–50 eV range.

The energy loss profiles for low-loss show the typical absorption peak near 25 eV for zirconium oxide. They are mapped within the defect colony, region “b,” and just outside it on both sides, “a” and “c.” The 25 eV peak, which is within the colony, shows a significant shift to the left as compared to the peaks from outside the defect colony. The shift is more clearly evident when the spectra are fit to Lorentzian forms and normalized with respect to the right-most peak in the spectrum, as shown on the bottom right in Figure 5B. The shift is attributed to the suboxide.⁶⁷ The shift suggests that the oxide in the defect colonies is highly reduced.⁶⁷

SAED data of interior defects are presented in Figure 6. The first, Figure 6A, refers to the reference site outside of

the defect colony, whereas Figure 6B lies within the defect colony. The diffraction patterns are aligned along the [1 0 0] zone axis.

The double-diffraction spots in Figure 6B indicate a second phase, which is epitaxial and coherent within the parent cubic crystal. This second phase represents the structure of the defect colonies.

In summary, the TEM results show that the defect colonies are a suboxide of zirconia. They are coherent with the parent single crystal; that is, they have grown epitaxially within the parent cubic structure, but with a smaller lattice parameter. They likely contribute to the electronic conductivity of the Ar-flashed single crystals.

3.2.2 | The surface layer

The surface layer that was reported in Figure 3A has features that are analogous to those seen within the defect

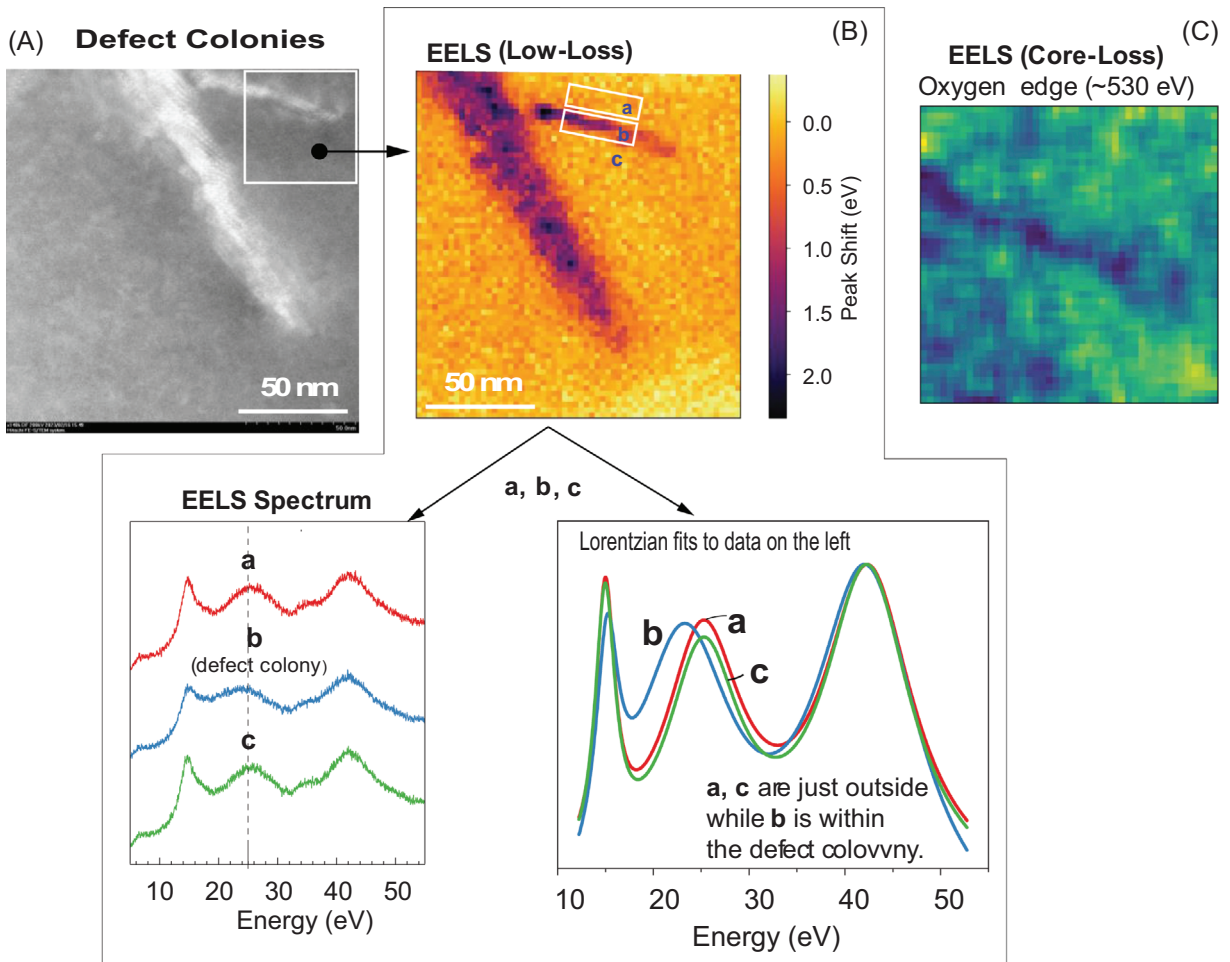


FIGURE 5 (A) Image of the defect colony. (B) EELS. Low-Loss EELS was shown by a map of the peak shifting at 25 eV, within the defect colony, relative to the peaks from just outside the defect colony. (C) The intensity map of the oxygen edge (~ 530 eV) in the Core-Loss EELS.

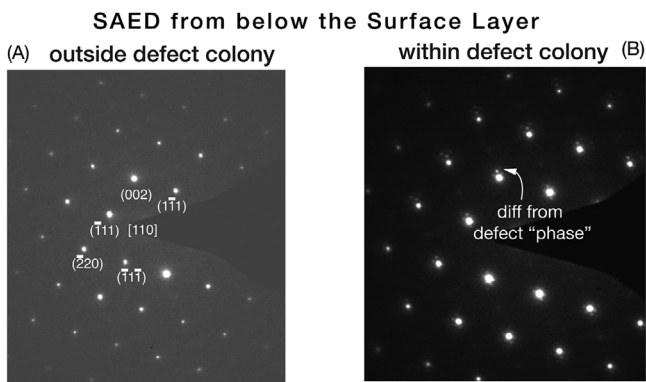


FIGURE 6 (A) Selected area electron diffraction (SAED) patterns from outside, (B) within the defect colony. The diffraction pattern (A) is consistent with cubic ZrO_2 .

colonies inside the crystal. However, here, the degree of non-stoichiometry is greater. Though still coherent with the cubic crystal, it has a significantly smaller lattice parameter, about 8% smaller than the parent crystal.

The EDS and EELS results from the surface layer are shown in Figure 7. The EDS line scans in Figure 7 on the left show a very significant loss of oxygen in the surface layer. The EELS spectra on the right taken from within a defect colony are given the following nomenclature:

- From the interior within the defect colony.
- And the interior outside the defect colony.
- From within the surface layer.

The shifts in the 25 eV peaks should be compared to B, which is from the clear region within the interior. The peak from the surface layer shifts more significantly to the left than the peak from the defect colony within the specimen interior, confirming that the defect concentration is much greater near the surface than within the defect colonies below the surface.

Note that the 25 eV peaks shift toward the Zr metallic spectrum.⁶⁷

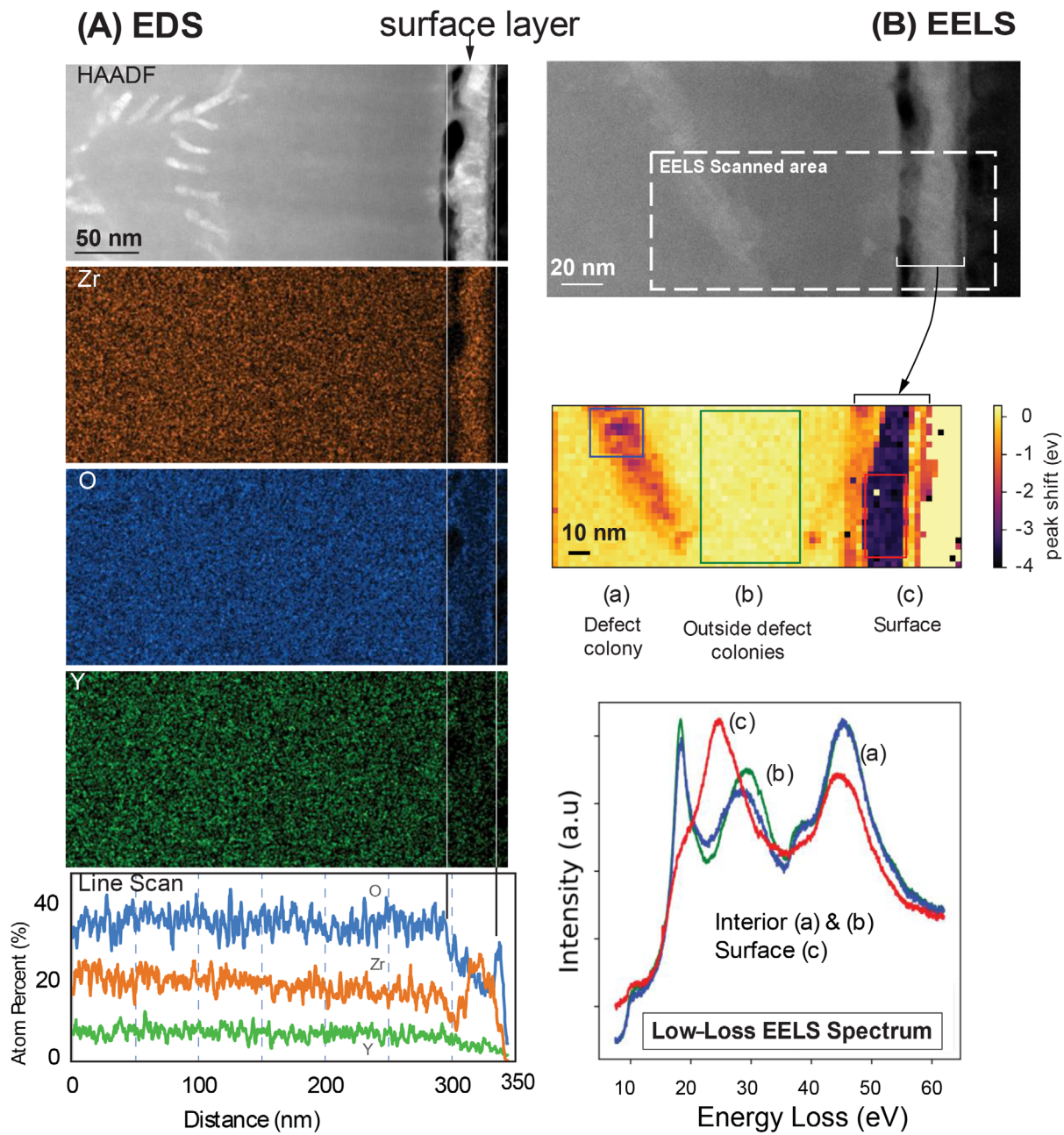


FIGURE 7 (A) EDS and (B) electron energy loss spectroscopy (EELS) spectra from Ar600. EDS maps and the line scan show severe oxygen deficiency in the surface layer. Low-loss EELS, in particular the shift in the peak near 25 eV from three regions: (a) the defect colony within the interior below the surface, (b) the interior, and (c) from the surface layer. The shift in the middle peak from the surface layer is severe—approaching the peak expected from metallic zirconium.

SAED from regions that include both the surface and the interior is shown in Figure 8. Two sets of diffraction spots are seen, both with the same structure and orientation, which are epitaxially related to one another, but one with a smaller lattice parameter. The patterns are similar to those seen in Figure 6B taken from the interior of the crystal, except that the diffraction angle for the spots from the second phase is slightly larger here, implying a smaller lattice parameter for the surface phase. The surface diffraction spots are also brighter than the diffraction

pattern from the interior, as shown in Figure 6B, implying a higher concentration of defects.

3.3 | X-ray of bulk specimens

The single crystals were examined by XRD. The XRD scan ranged from 10° to 130° in steps of 0.01° . The main information is obtained from the plots that contain diffraction from $(2\ 0\ 0)$ and $(4\ 0\ 0)$ planes, given in Figure 9; they

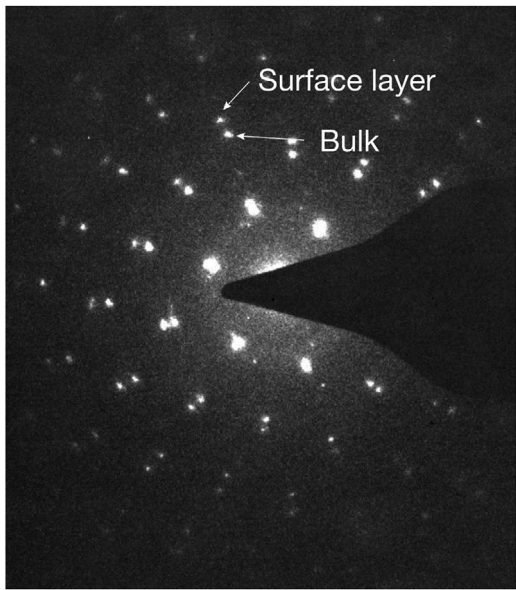


FIGURE 8 Single-crystal selected area electron diffraction (SAED) from within the interior together with diffraction from the surface layer. The surface structure is epitaxially coherent with the parent crystal, but with an 8% smaller lattice parameter.

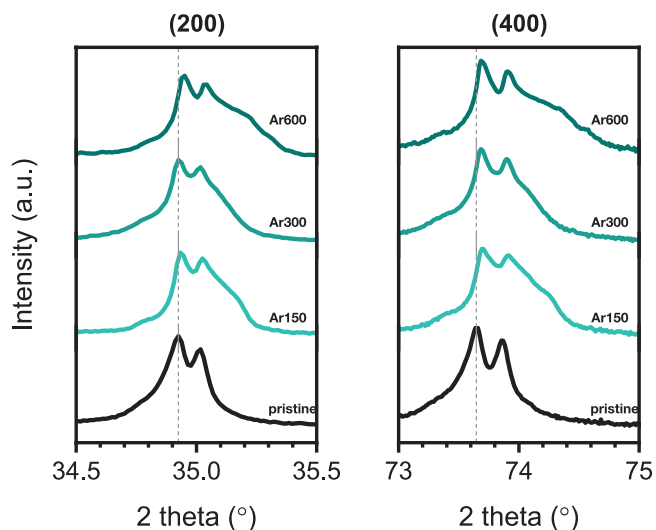


FIGURE 9 The X-ray diffraction patterns from specimens flashed at three current levels. Note that (1 0 0) peaks shift to the higher angle, indicating the reduction of the lattice parameter. In addition, there are extra peaks at the shoulder of main peaks.

show strong peaks at 34.9° and 73.6° , respectively. Diffraction from four specimens, pristine, Ar150, Ar300, and Ar600, is presented. The flashed specimens show shifts in the main peaks and extra peaks on the right shoulder of the main peaks. The computed lattice parameter and the strain calculated from these shoulder peaks are presented in Table 1.

TABLE 1 The lattice parameters and microstrains (within the bulk) obtained from X-ray diffraction data in Figure 9.

Sample	a [Å] (Microstrains calculated from the shoulder peaks)		
	Main (100) peak	Shoulder peak I	Shoulder peak II
Pristine	5.145		
Ar150	5.142	$5.139 (3.1 \times 10^{-4})$	$5.130 (5 \times 10^{-4})$
Ar300	5.142	$5.135 (6.1 \times 10^{-4})$	
Ar600	5.143	$5.141 (2.5 \times 10^{-4})$	$5.126 (10.6 \times 10^{-4})$

Note: The shoulder peaks arise from the defect colonies bearing a significant strain with respect to the mother crystal. Not listed here is the lattice parameter from the surface layer measured in transmission electron microscopy, which was 8% smaller than the cubic crystal.

The lattice parameter of YSZ depends on the amount of the yttria⁶⁸ due to the introduction of oxygen vacancies. However, it has been reported that the lattice parameter is not significantly changed by the blackening of zirconia.⁶⁹ Lebrun et al.⁹ observed *lattice expansion* in YSZ by in situ synchrotron XRD. Ab initio calculations⁹ suggest that the lattice expansion arose from Frenkel defects (vacancy-interstitial pairs).

Here we note that the flash reaction in the Ar atmosphere produces a suboxide by removing oxygen from its normal sites without compensation with oxygen atoms at the interstitial site. So, unlike Lebrun's in situ XRD,⁹ which was carried out in air, the specimens flashed in Ar show a significant loss of oxygen ions. This difference between experiments carried out in ambient air and in Ar atmosphere is likely related to the paucity of oxygen in Ar.

In summary, the XRD patterns confirm the secondary diffraction spots seen in SAED in the electron microscope. The higher resolution of XRD from bulk specimens has allowed measurements of the lattice parameter of the defect colonies that appear as a second phase, described as shoulder peaks in Table 1. These second phases are epitaxial with the parent phase but have a smaller lattice parameter; they have been translated into microstrains.

3.4 | Raman spectroscopy

Raman spectra from the pristine and Ar600 samples are shown in Figure 10. The pristine sample shows the typical signals of single crystal 8YSZ.⁷⁰ The most intense signals at 149 cm^{-1} , and 614 cm^{-1} can be assigned to the cubic YSZ phase.⁷⁰ The broad signals between 200 and 400 cm^{-1} and a small signal at 480 cm^{-1} can often be found in 8YSZ samples.^{70–72} They correspond to the tetragonal YSZ phase due to an insufficient Y stabilization content; this is characteristic for the tetragonal YSZ phase and, therefore,

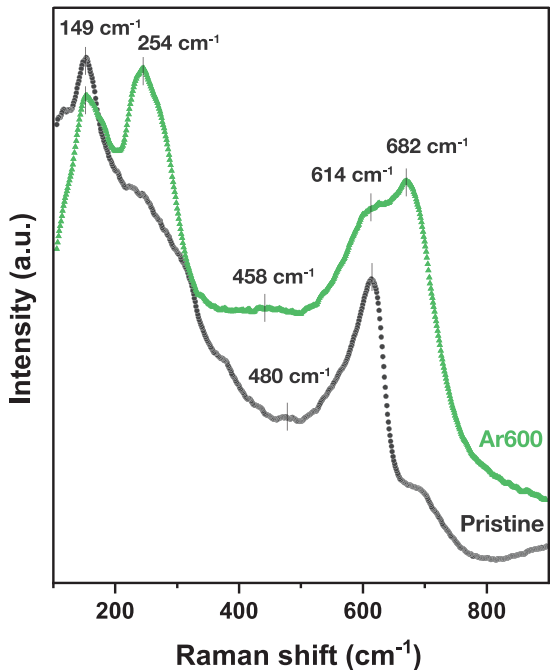


FIGURE 10 Raman spectra from the pristine and Ar600 sample.

suggests that the sample is not fully stabilized in the cubic phase.^{70–72}

The Ar600 specimen shows broadened and extra peaks. The deconvoluted spectra show five Raman shifts at 149, 254, 458, 614, and 682 cm⁻¹. The peaks at 149 and 614 cm⁻¹ can be again assigned to the cubic 8YSZ phase.⁷⁰ The peaks at 254, 458, and 682 cm⁻¹ arise from flash event.

In previous reports, additional broad signals were found in ion-irradiated zirconia samples that were explained by high structural disorder.⁷³ Therefore, the signal at 682 cm⁻¹ could be attributed to a disorder in the oxygen atoms or defect-induced vibration mode.⁷³ The Raman shift of the disordered oxygen atom depends strongly on the YSZ structure; in tetragonal YSZ, it will occur at 615 and 700 cm⁻¹, whereas it will be present at around 640 cm⁻¹ in the cubic YSZ.⁷³ Therefore, if the 682 cm⁻¹ signal belongs to a disorder in the oxygen lattice, it also indicates the presence of the tetragonal phase in the sample. Consequently, the signals at 254 and 458 cm⁻¹ can be associated with the tetragonal phase, as the tetragonal zirconia has six Raman active modes ($1A_{1g} + 3E_g + 2B_{1g}$) at around 145, 268, 314, 463, 604, and 639 cm⁻¹.⁷⁴ The vibrational mode of each peak is under debate. The peak at 268 cm⁻¹ is considered E_g^{74,75} or A_{1g},⁷⁶ whereas the signal at 463 cm⁻¹ is considered E_g^{74,76} or B_{1g}.⁷⁵

Therefore, it is difficult to develop mechanistic hypotheses of the signal generation at 254 and 458 cm⁻¹. As we now know that the sample has defect colonies, we propose that the signals at 254 and 458 cm⁻¹ also arise

from the structural defects that are significantly deficient in oxygen. The high concentration of oxygen vacancies in these colonies can be expected to alter the vibration mode.

3.5 | Optical microscopy

The results presented in this section were obtained by the authors: SJ and RR. The experiments were performed in Boulder, CO. They are cognizant of the unusual nature of the results, which may be subject to different interpretations. We hope that further discussion of these interesting results will emerge in future publications of flash in single crystals.

When the surface layer (approximately 50 μm) was removed by mechanical polishing, we discovered cracks across the specimen, which are shown in Figure 11A. The cracks were connected, stretching across the full gage length between the electrodes. As these colonies were shown to have a smaller lattice parameter, there would have been tensile strain locally. It is inferred that local strains evolved into microcracks during mechanical polishing. The crack can be seen in an SEM micrograph shown in Figure 10B. As the TEM specimens now show evidence of a crack network, it may be concluded that the cracks were formed during mechanical polishing, which exacerbated the effect of the microstrains between the defect colonies and the parent crystal. It is still surprising that the sample held together despite the network of cracks. Given the history of cracks being related to the defect colonies, it is suggested that the crack surfaces harbored a surface charge, therefore, acting like capacitors. The capacitor plates exert an attraction toward each other when charged. The separating force from lattice microstrains is balanced by the attraction between the crack surfaces.⁷⁷

Despite the cracks, the specimens remained mildly conductive. The conductivities with and without polishing are reported in Figure 11C. The change in the thickness of the sample, with and without the mechanical removal of the surface was just ~3%, yet the conductivity (in the parallel direction) drops from ~200 S m⁻¹ down to 10 S m⁻¹. Extrapolation from the rule of mixtures would suggest that the conductivity of the surface was approximately $(100/3) \times (200/10) = 670$ times greater. But even this would be an underestimate since the thickness of the surface layer was ~30 nm, whereas the thickness that was removed was approximately 50 μm, which is more than 1000 times greater than the thickness of the surface layer (30 nm) measured in the TEM. Therefore, strictly speaking, the rule of mixtures would predict that the surface layer is 670 000 times more conducting than the

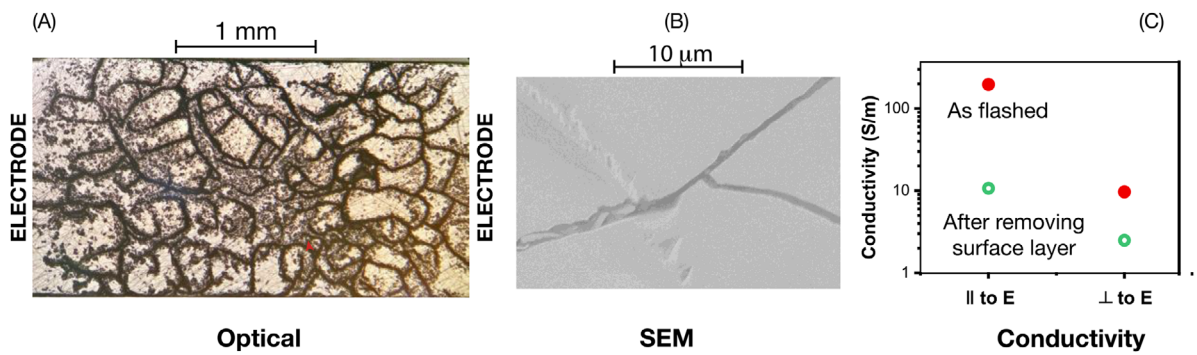


FIGURE 11 (A) Optical image of the Ar600 specimen. The image was captured after polishing the surface to a depth of about 50 μm ; (B) SEM image shown the network on the left near the lines in the polished sample (the sample was polished with a fine cloth dispersed with 0.02 mm particles of alumina); (C) conductivity before and after removing the surface layer by mechanical polishing.

bulk. Such a large difference in the conductivities of the surface and the bulk is not comprehensible.

The conductivity of the specimen can be assumed to consist of three parts: (a) the surface layer, (b) the conductivity of the interconnected defect colonies, and (c) the conductivity of the remaining matrix outside of the defect colonies. After mechanical polishing, the surface layer contribution (a) is removed, whereas (c) the conductivity of the matrix without the defect colonies remains intact. We assume here that the conductivity of the defect colonies, which are now cracked and separated, is degraded in the polished specimen. With this assumption, it is inferred that the conductivity of the polished specimen represents the conductivity of the matrix without the benefit of the defect colonies. We infer that the conductivity of the polished samples is reflecting the conductivity of these “defect-free” regions.

Also of note is that the density of cracks is greater in the middle of the specimen. The cause and the significance of this observation are unclear at the present time. The possible reason at this point is that the higher density of crack region is related to the junction among oppositely charged areas, such as the p-n junction^{50,78,79}; it has been proposed that as p- and n-type conductivity is introduced by the flash reaction.

4 | DISCUSSION

The following results from a single crystal of cubic zirconia flashed and cooled within Ar atmosphere are noteworthy. The crystal remains electronically conducting.

- (i) Large colonies of a suboxide of zirconia embedded epitaxially within the parent cubic structure have been identified. Furthermore, the parent cubic crystal is also oxygen-deficient, but to a much lesser degree than the defect colonies.

- (ii) The suboxide phase is driven by the colossal concentrations of oxygen vacancies produced by flash. (The density of oxygen vacancies is related to the current density.⁸⁰) The suboxide is structurally coherent with the parent cubic crystal. Its lattice parameter is up to 8% smaller than the parent crystal. The dendritic structure of the suboxide is suggestive of a nucleation and growth process.
- (iii) The colossal concentrations of oxygen vacancies mean that they are now a species by themselves. It may now be possible to construct phase diagrams where one of the phases is the suboxide. Thus, concepts for a new far-from-equilibrium thermodynamics start to emerge.
- (iv) A 30 nm thick surface layer develops that is severely oxygen deficient but still coherent with the cubic structure of the parent crystal.
- (v) The microstrains in the suboxide cause microcracks when the crystal is mechanically polished. However, the crystal remains electronically conductive, though with only 5% of the conductivity of the unpolished sample. This remanent conductivity is attributed to the conductivity of the matrix outside the defect colonies.

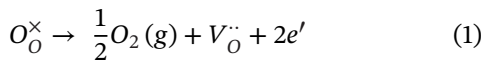
The results presented here are specific to the flash experiment carried out in Ar atmosphere with an oxygen partial pressure of 10^{-5} to 10^{-4} . Nevertheless, they share a common feature of flash experiments, which is a transition to highly conductive electronic behavior at the onset of flash.

How the suboxide is formed in flash remains an open question. The electrical fields are far too low (amounting to a few tens of meV) to overcome the formation energy of defects. The role of phonons that has been discussed⁵³ continues to remain of essence.

Although the present flash experiments were carried out in Ar, similar behavior is seen in ambient air, that is a rise in electronic conductivity at the onset of flash, which can be

retained by quenching in liquid nitrogen.⁵⁷ However, the specimens return to their insulating state when they are furnace-cooled in ambient air. The reversion to the insulating state may be explained by the replacement of oxygen vacancies by oxygen ions drawn in from the atmosphere—that is, the reverse of the reaction given in Equation (1) below.

The conductivity of the Ar specimens can be explained by the formation of oxygen vacancies, which release electrons according to⁸¹



The great unanswered question is the delocalization of the electrons created by the above reaction. DFT calculations are needed to estimate the Fermi level of the electrons in the suboxide. Further, the participation of the zirconium ions in the overall electronic structure of the suboxide remains a question.

The interest in electroluminescence, a common feature of flash, has been renewed by the finding that an overlay of magnetic fields causes the flash to migrate from the surface of a flashing specimen into a free-standing workpiece without electrodes.⁸¹ It is possible that the luminescence is produced by an evanescent plasma present adjacent to surface. The highly conductive surface reported in the present study may be a consequence of such an effect.

The present experiments point to the need for characterization of the defect structure in different ways, most importantly by TEM. Much further work on different material systems is needed.

5 | CONCLUSIONS

Cubic zirconia was flashed and cooled in Ar atmosphere. It yielded a highly conducting specimen. EDS and EELS characterizations in the TEM revealed areas of interlaced colonies of oxygen-deficient oxide. These colonies were epitaxially related to the parent crystal but with a smaller lattice parameter. This suboxide, consisting of a large concentration of oxygen vacancies, is held to have contributed to the electronic conductivity. The regions outside these colonies were also somewhat oxygen-deficient and therefore would have been electronically conducting, but much less so than the defect colonies.

The (1 0 0) surface was examined in detail by TEM. The surface layer was epitaxial with the parent crystal but with a lattice contraction of 8%. It was severely oxygen-deficient. The low-loss EELS spectra showed leftward shift in the peak normally positioned at ~25 eV. The shift was so large as to approach the peak expected from metallic zirconium.

Ab initio calculations for the electronic structure of the suboxide as a function of the lattice contraction are highly recommended. These calculations can shed light on the mechanism of electronic conductivity in flash experiments.

The reader is cautioned that the present experiments were carried out in Ar. In Ar, the oxygen vacancies cannot be neutralized for kinetic reasons. However, the vacancies are refilled by inward diffusion of oxygen from the environment during furnace-cool down in ambient air, which erases the electronic conductivity of the specimen.

ACKNOWLEDGMENTS

Support from the German Research Foundation DFG in the framework of the priority program “Fields Matter” (SPP 1959) is gratefully acknowledged. The authors acknowledge the support of Hitachi High-Technologies for providing access to and expertise regarding the HF5000 S/TEM. DJ acknowledges the support of the DFG via the Emmy Noether Programme (Rh 146/1-1.). MK acknowledges the support of the DFG via the project MA 1280/69-1. SJ and RR thank the Office of Naval Research for supporting this research under grant N00014-18-1-2270. We appreciate Dr. Antti Makinen for taking an interest in this project.

ORCID

Seohyeon Jo  <https://orcid.org/0000-0002-4614-7281>

Moritz Kindelmann  <https://orcid.org/0000-0001-9676-2090>

Yoo Jung Sohn  <https://orcid.org/0000-0002-7994-7269>

Walter Sebastian Scheld  <https://orcid.org/0000-0003-0692-2404>

Olivier Guillon  <https://orcid.org/0000-0003-4831-5725>

Rishi Raj  <https://orcid.org/0000-0001-8556-9797>

REFERENCES

1. Katz JD. Microwave sintering of ceramics. *Annu Rev Mater Sci*. 1992;22(1):153–70. <https://doi.org/10.1146/annurev.ms.22.080192.001101>
2. Grasso S, Sakka Y, Maizza G. Electric current activated/assisted sintering (ECAS): a review of patents 1906–2008. *Sci Technol Adv Mater*. 2009;10(5):053001. <https://doi.org/10.1088/1468-6996/10/5/053001>
3. Anselmi-Tamburini U, Gennari S, Garay JE, Munir ZA. Fundamental investigations on the spark plasma sintering/synthesis process. *Mater Sci Eng A*. 2005;394(1–2):139–48. <https://doi.org/10.1016/j.msea.2004.11.019>
4. Tokita M. Progress of spark plasma sintering (SPS) method, systems, ceramics applications and industrialization. *Ceramics*. 2021;4(2):160–98. <https://doi.org/10.3390/ceramics4020014>
5. Grasso S, Saunders T, Porwal H, Milsom B, Tudball A, Reece M. Flash spark plasma sintering (FSPS) of α and β SiC. *J Am Ceram Soc*. 2016;99(5):1534–43. <https://doi.org/10.1111/jace.14158>

6. Guillou O, Gonzalez-Julian J, Dargatz B, Kessel T, Schierning G, Räthel J, et al. Field-assisted sintering technology/spark plasma sintering: mechanisms, materials, and technology developments. *Adv Eng Mater.* 2014;16(7):830–49. <https://doi.org/10.1002/adem.201300409>
7. Cologna M, Rashkova B, Raj R. Flash sintering of nanograin zirconia in <5 s at 850°C. *J Am Ceram Soc.* 2010;93(11):3556–59. <https://doi.org/10.1111/j.1551-2916.2010.04089.x>
8. Terauds K, Lebrun J-M, Lee H-H, Jeon TY, Lee SH, Je J H, et al. Electroluminescence and the measurement of temperature during Stage III of flash sintering experiments. *J Eur Ceram Soc.* 2015;35(11):3195–99. <https://doi.org/10.1016/j.jeurceramsoc.2015.03.040>
9. Lebrun JM, Hellberg CS, Jha SK, Kriven WM, Steveson A, Seymour KC, et al. In-situ measurements of lattice expansion related to defect generation during flash sintering. *J Am Ceram Soc.* 2017;100(11):4965–70. <https://doi.org/10.1111/jace.15071>
10. Lebrun JM, Morrissey TG, Francis JSC, Seymour KC, Kriven WM, Raj R. Emergence and extinction of a new phase during on-off experiments related to flash sintering of 3YSZ. *J Am Ceram Soc.* 2015;98(5):1493–97. <https://doi.org/10.1111/jace.13476>
11. Gil-González E, Pérez-Maqueda L, Sánchez-Jiménez P, Perejón A. Flash sintering research perspective: a bibliometric analysis. *Mater Basel.* 2022;15(2):416. <https://doi.org/10.3390/ma15020416>
12. Prette ALG, Cologna M, Sglavo V, Raj R. Flash-sintering of Co_2MnO_4 spinel for solid oxide fuel cell applications. *J Power Sources.* 2011;196(4):2061–65. <https://doi.org/10.1016/j.jpowsour.2010.10.036>
13. Cologna M, Prette ALG, Raj R. Flash-sintering of cubic yttria-stabilized zirconia at 750°C for possible use in SOFC manufacturing. *J Am Ceram Soc.* 2011;94(2):316–19. <https://doi.org/10.1111/j.1551-2916.2010.04267.x>
14. Hao X, Liu Y, Wang Z, Qiao J, Sun K. A novel sintering method to obtain fully dense gadolinia doped ceria by applying a direct current. *J Power Sources.* 2012;210:86–91. <https://doi.org/10.1016/j.jpowsour.2012.03.006>
15. Karakuscu A, Cologna M, Yarotski D, Won J, Francis JSC, Raj R, et al. Defect structure of flash-sintered strontium titanate. *J Am Ceram Soc.* 2012;95(8):2531–36. <https://doi.org/10.1111/j.1551-2916.2012.05240.x>
16. M'Peko J-C, Francis JSC, Raj R. Field-assisted sintering of undoped BaTiO_3 : microstructure evolution and dielectric permittivity. *J Eur Ceram Soc.* 2014;34(15):3655–60.
17. Schmerbauch C, Gonzalez-Julian J, Röder R, Ronning C, Guillou O. Flash sintering of nanocrystalline zinc oxide and its influence on microstructure and defect Formation. *J Am Ceram Soc.* 2014;97(6):1728–35. <https://doi.org/10.1111/jace.12972>
18. Yoshida H, Hayasaka H, Soga K, Morita K, Kim B-N, Yamamoto T. Doping effect on the flash sintering of Y_2O_3 : promotion of densification and optical translucency. *J Eur Ceram Soc.* 2020;40(15):6053–60. <https://doi.org/10.1016/j.jeurceramsoc.2020.06.041>
19. Kumar A, Sharma G, Aftab A, Ahmad MI. Flash assisted synthesis and densification of five component high entropy oxide ($\text{Mg, Co, Cu, Ni, Zn}$)O at 350°C in 3 min. *J Eur Ceram Soc.* 2020;40(8):3358–62. <https://doi.org/10.1016/j.jeurceramsoc.2020.02.036>
20. Martinez JM, Biesuz M, Dong J, Gauna M., Suarez G., Sglavo VM, et al. Flash sintering of zircon: rapid consolidation of an ultrahigh bandgap ceramic. *J Asian Ceram Soc.* 2021;9(1):374–81. <https://doi.org/10.1080/21870764.2020.1869882>
21. Gil-González E, Perejón A, Sánchez-Jiménez PE, Sayagués MJ, Raj R, Pérez-Maqueda LA. Phase-pure BiFeO_3 produced by reaction flash-sintering of Bi_2O_3 and Fe_2O_3 . *J Mater Chem A.* 2018;6(13):5356–66. <https://doi.org/10.1039/c7ta09239c>
22. Grasso S, Saunders T, Porwal H, Cedillos-Barraza O, Jayaseelan DD, Lee WE, et al. Flash spark plasma sintering (FSPS) of pure ZrB_2 . *J Am Ceram Soc.* 2014;97(8):2405–8. <https://doi.org/10.1111/jace.13109>
23. Ito M, Kawahara K. Synthesis of thermoelectric Mg_2Si by reactive sintering utilizing directly applied current sintering. *Mater Trans.* 2015;56(12):2023–28. <https://doi.org/10.2320/matertrans.Y-M2015829>
24. Ingraci Neto RR, Raj R. The flash effect in electronic conductors: the case of amorphous carbon fibers. *Scr Mater.* 2020;179:20–24. <https://doi.org/10.1016/j.scriptamat.2020.01.003>
25. Saunders T, Grasso S, Reece MJ. Ultrafast-contactless flash sintering using plasma electrodes. *Sci Rep.* 2016;6(1):27222. <https://doi.org/10.1038/srep27222>
26. Bicer H. Time-resolved in-situ analysis of densification of nanoboron carbide under superimposed electric and thermal fields with energy dispersive X-ray diffraction. Rutgers The State University of New Jersey, School of Graduate Studies; 2016
27. Zapata-Solvas E, Bonilla S, Wilshaw PR, Todd RI. Preliminary investigation of flash sintering of SiC. *J Eur Ceram Soc.* 2013;33(13–14):2811–16. <https://doi.org/10.1016/j.jeurceramsoc.2013.04.023>
28. McWilliams B, Yu J, Kellogg F, Kilczewski S. Enhanced sintering kinetics in aluminum alloy powder consolidated using DC electric fields. *Metall Mater Trans Phys Metall Mater Sci.* 2017;48(2):919–29. <https://doi.org/10.1007/s11661-016-3861-4>
29. Yu M, Grasso S, Mckinnon R, Saunders T, Reece MJ. Review of flash sintering: materials, mechanisms and modelling. *Adv Appl Ceram.* 2017;116(1):24–60. <https://doi.org/10.1080/17436753.2016.1251051>
30. Biesuz M, Sglavo VM. Flash sintering of ceramics. *J Eur Ceram Soc.* 2019;39(2–3):115–43. <https://doi.org/10.1016/j.jeurceramsoc.2018.08.048>
31. Wang C, Ping W, Bai Q, Cui H, Hensleigh R, Wang R, et al. A general method to synthesize and sinter bulk ceramics in seconds. *Science.* 2020;368(6490):521–26. <https://doi.org/10.1126/science.aaz7681>
32. Raj R, Wolf DE, Yamada CN, Jha SK, Lebrun J. On the confluence of ultrafast high-temperature sintering and flash sintering phenomena. *J Am Ceram Soc.* 2023;106(7):3983–98. <https://doi.org/10.1111/jace.19070>
33. Raj R. Joule heating during flash-sintering. *J Eur Ceram Soc.* 2012;32(10):2293–301. <https://doi.org/10.1016/j.jeurceramsoc.2012.02.030>
34. Cologna M, Francis JSC, Raj R. Field assisted and flash sintering of alumina and its relationship to conductivity and MgO-doping. *J Eur Ceram Soc.* 2011;31(15):2827–37. <https://doi.org/10.1016/j.jeurceramsoc.2011.07.004>
35. Raj R, Cologna M, Francis JSC. Influence of externally imposed and internally generated electrical fields on grain growth, diffusional creep, sintering and related phenomena in ceramics. *J Am Ceram Soc.* 2011;94(7):1941–65. <https://doi.org/10.1111/j.1551-2916.2011.04652.x>

36. Francis JSC, Raj R. Flash-sinterforging of nanograin zirconia: field assisted sintering and superplasticity. *J Am Ceram Soc.* 2012;95(1):138–46. <https://doi.org/10.1111/j.1551-2916.2011.04855.x>
37. Francis JSC, Cologna M, Montinaro D, Raj R. Flash sintering of anode-electrolyte multilayers for SOFC applications. *J Am Ceram Soc.* 2013;96(5):1352–54. <https://doi.org/10.1111/jace.12330>
38. Pereira Da Silva JG, Lebrun JM, Al-Qureshi HA, Janssen R, Raj R. Temperature distributions during flash sintering of 8% yttria-stabilized zirconia. *J Am Ceram Soc.* 2015;98(11):3525–28. <https://doi.org/10.1111/jace.13786>
39. Jongmanns M, Wolf DE. Element-specific displacements in defect-enriched TiO_2 : indication of a flash sintering mechanism. *J Am Ceram Soc.* 2020;103(1):589–96. <https://doi.org/10.1111/jace.16696>
40. Kathiria R, Wolf DE, Raj R, Jongmanns M. Frenkel pairs cause elastic softening in zirconia: theory and experiments. *New J Phys.* 2021;23(5):053013.
41. Raj R, Kulkarni A, Lebrun J-M, Jha S. Flash sintering: a new frontier in defect physics and materials science. *MRS Bull.* 2021;46(1):36–43. <https://doi.org/10.1557/s43577-020-00011-1>
42. Narayan J. Grain growth model for electric field-assisted processing and flash sintering of materials. *Scr Mater.* 2013;68(10):785–88. <https://doi.org/10.1016/j.scriptamat.2013.01.008>
43. Chaim R, Estournès C. On thermal runaway and local endothermic/exothermic reactions during flash sintering of ceramic nanoparticles. *J Mater Sci.* 2018;53(9):6378–89. <https://doi.org/10.1007/s10853-018-2040-y>
44. Corapcioglu G, Gulgum MA, Kisslinger K, Sturm S, Jha SK, Raj R. Microstructure and microchemistry of flash sintered $K_{0.5}Na_{0.5}NbO_3$. *J Ceram Soc Jpn.* 2016;124(4):321–28. <https://doi.org/10.2109/jcersj2.124.p4-1>
45. Chaim R, Chevallier G, Weibel A, Estournès C. Flash sintering of dielectric nanoparticles as a percolation phenomenon through a softened film. *J Appl Phys.* 2017;121(14):145103. <https://doi.org/10.1063/1.4980853>
46. Chaim R. Particle surface softening as universal behaviour during flash sintering of oxide nano-powders. *Materials.* 2017;10(2):179. <https://doi.org/10.3390/ma10020179>
47. Downs JA. Mechanisms of flash sintering in cubic zirconia. PhD Thesis. Università degli studi di Trento; 2013
48. Mishra TP, Neto RRI, Speranza G, Quaranta A, Sglavo VM, Raj R, et al. Electronic conductivity in gadolinium doped ceria under direct current as a trigger for flash sintering. *Scr Mater.* 2020;179:55–60. <https://doi.org/10.1016/j.scriptamat.2020.01.007>
49. Kirchheim R. On the mixed ionic and electronic conductivity in polarized yttria stabilized zirconia. *Solid State Ionics.* 2018;320:239–58. <https://doi.org/10.1016/j.ssi.2018.03.014>
50. Jovani M, Beltrán-Mir H, Cordoncillo E, West AR. Field-induced p-n transition in yttria-stabilized zirconia. *Sci Rep.* 2019;9(1):18538. <https://doi.org/10.1038/s41598-019-54588-y>
51. Charalambous H, Jha SK, Okasinski JS, Tsakalakos T. Generation of electric-field stabilized zirconium monoxide secondary phase within cubic zirconia. *Scr Mater.* 2021;190:22–26. <https://doi.org/10.1016/j.scriptamat.2020.08.026>
52. Itoh A, Tokunaga T, Kodaira A, Yoshida H, Yamamoto T. Variation of photoluminescence intensity depending on the timing of electric field application during isothermal flash sintering for 3mol% Y_2O_3 – ZrO_2 polycrystal. *Ceram Int.* 2022;48(19):28712–17. <https://doi.org/10.1016/j.ceramint.2022.06.185>
53. Jongmanns M, Raj R, Wolf DE. Generation of Frenkel defects above the Debye temperature by proliferation of phonons near the Brillouin zone edge. *New J Phys.* 2018;20(9):093013. <https://doi.org/10.1088/1367-2630/aadd5a>
54. Mishra TP, Neto RRI, Raj R, Guillon O, Bram M. Current-rate flash sintering of gadolinium doped ceria: microstructure and defect generation. *Acta Mater.* 2020;189:145–53. <https://doi.org/10.1016/j.actamat.2020.02.036>
55. Francis JSC, Raj R. Influence of the field and the current limit on flash sintering at isothermal furnace temperatures. *J Am Ceram Soc.* 2013;96(9):2754–58. <https://doi.org/10.1111/jace.12472>
56. Jo S, Raj R. Transition to electronic conduction at the onset of flash in cubic zirconia. *Scr Mater.* 2020;174:29–32. <https://doi.org/10.1016/j.scriptamat.2019.07.043>
57. Kathiria RK, Jo S, Raj R, Yadav D. In-flash immersion-and-quench of yttria-stabilized zirconia into liquid nitrogen yields an electronic conductor. *J Am Ceram Soc.* 2022;105(3):1635–39. <https://doi.org/10.1111/jace.18210>
58. Jo S, Jalali SIA, Raj R. Flash in argon atmosphere yields electronically conducting yttria-stabilized zirconia at ambient temperature. *J Am Ceram Soc.* 2023;106(9):5133–39. <https://doi.org/10.1111/jace.19166>
59. Jo S, Lee M, Leahy IA, Vendrell X, Raj R. Capacitive discharge in flash experiments: a discussion of the charged species. *J Am Ceram Soc.* 2023;106(10):5635–41. <https://doi.org/10.1111/jace.19250>
60. Masó N, West AR. Electronic conductivity in yttria-stabilized zirconia under a small dc bias. *Chem Mater.* 2015;27(5):1552–58. <https://doi.org/10.1021/cm503957x>
61. Wang H, Phuah XL, Charalambous H, Jha SK, Li J, Tsakalakos T, et al. Staged microstructural study of flash sintered titania. *Materialia.* 2019;8:100451. <https://doi.org/10.1016/j.mtla.2019.100451>
62. Wang H, Phuah XL, Li J, Holland TB, Vikrant KSN, Li Q, et al. Key microstructural characteristics in flash sintered 3YSZ critical for enhanced sintering process. *Ceram Int.* 2019;45(1):1251–57. <https://doi.org/10.1016/j.ceramint.2018.10.007>
63. Rheinheimer W, Phuah XL, Wang H, Lemke F, Hoffmann MJ, Wang H. The role of point defects and defect gradients in flash sintering of perovskite oxides. *Acta Mater.* 2019;165:398–408. <https://doi.org/10.1016/j.actamat.2018.12.007>
64. Schwarzbach D, Gonzalez-Julian J, Guillon O, Roddatis V, Volkert CA. Towards in-situ electron microscopy studies of flash sintering. *Ceramics.* 2019;2(3):472–87. <https://doi.org/10.3390/ceramics2030036>
65. Peña de la F, Prestat E, Fauske VT, Burdet P, Lähnemann J, Jokubauskas P, et al. hyperspy/hyperspy: release v1.7.3. Zenodo; 2022.
66. Liao Y. Practical electron microscopy and database. 2006. <http://www.globalsino.com/EM/>
67. Nicholls RJ, Ni N, Lozano-Perez S, London A, McComb DW, Nellist PD, et al. Crystal structure of the ZrO phase at zirconium/zirconium oxide interfaces. *Adv Eng Mater.* 2015;17(2):211–15. <https://doi.org/10.1002/adem.201400133>
68. Ingel RP, Lewis D III. Lattice parameters and density for Y_2O_3 -stabilized ZrO_2 . *J Am Ceram Soc.* 1986;69(4):325–32. <https://doi.org/10.1111/j.1551-2916.1986.tb04741.x>
69. Wright DA, Thorp JS, Aypar A, Buckley HP. Optical absorption in current-blackened yttria-stabilized zirconia. *J Mater Sci.* 1973;8(6):876–82. <https://doi.org/10.1007/BF02397918>

70. Lomonova EE, Agarkov DA, Borik MA, Koraleva GM, Kulebyakin AV, Kuritsyna IE, et al. Structure and transport characteristics of single-crystal and ceramic $ZrO_2-Y_2O_3$ solid electrolytes. *Russ J Electrochem.* 2022;58(2):105–13. <https://doi.org/10.1134/s1023193522020069>
71. Yashima M, Ohtake K, Kakihana M, Arashi H, Yoshimura M. Determination of tetragonal-cubic phase boundary of $Zr_{1-x}R_xO_{2-x}$ ($R = Nd, Sm, Y, Er$ and Yb) by Raman scattering. *J Phys Chem Solids.* 1996;57(1):17–24.
72. Hemberger Y, Wichtner N, Berthold C, Nickel KG. Quantification of yttria in stabilized zirconia by Raman spectroscopy. *Int J Appl Ceram Technol.* 2016;13(1):116–24. <https://doi.org/10.1111/ijac.12434>
73. Ciszak C, Mermoux M, Gutierrez G, Leprêtre F, Duriez C, Popa I, et al. Raman spectra analysis of ZrO_2 thermally grown on Zircaloy substrates irradiated with heavy ion: effects of oxygen isotopic substitution. *J Raman Spectrosc.* 2019;50(3):425–35. <https://doi.org/10.1002/jrs.5513>
74. Fernández López E, Sánchez Escribano V, Panizza M, Carnasciali MM, Busca G. Vibrational and electronic spectroscopic properties of zirconia powders. *J Mater Chem.* 2001;11(7):1891–97. <https://doi.org/10.1039/b100909p>
75. Naumenko A, Berezovska N, Biliy M, Shevchenko OV. Vibrational analysis and Raman spectra of tetragonal zirconia. *Phys Chem Solid State.* 2008;9(1):121–25.
76. Quintard PE, Barbéris P, Mirgorodsky AP, Merle-Méjean T. Comparative lattice-dynamical study of the Raman spectra of monoclinic and tetragonal phases of zirconia and hafnia. *J Am Ceram Soc.* 2004;85(7):1745–49. <https://doi.org/10.1111/j.1151-2916.2002.tb00346.x>
77. Cheng DK. Fundamentals of engineering electromagnetics. 1st ed. Pearson Education: Reading, Mass: Pearson; 2019
78. Weppner W. Electronic transport properties and electrically induced pn junction in $ZrO_2 + 10 m/o Y_2O_3$. *J Solid State Chem.* 1977;20(3):305–14.
79. Vendrell X, West AR. Induced p-type semiconductivity in yttria-stabilized zirconia. *J Am Ceram Soc.* 2019;102(10):6100–6106. <https://doi.org/10.1111/jace.16492>
80. Rickert H. *Electrochemistry of solids: an introduction.* Berlin: Springer Science & Business Media; 2012.
81. Jalali SIA, Raj R. Touch-free flash sintering with magnetic induction within a reactor activated by the usual flash method. *J Am Ceram Soc.* 2022;105(11):6517–22. <https://doi.org/10.1111/jace.18601>

SUPPORTING INFORMATION

Additional supporting information can be found online in the Supporting Information section at the end of this article.

How to cite this article: Jo S, Kindelmann M, Jennings D, Balice L, Sohn YJ, Scheld WS, et al. Flash-induced defects in single-crystal 8YSZ characterized by TEM, XRD, and Raman spectroscopy. *J Am Ceram Soc.* 2024;1–15. <https://doi.org/10.1111/jace.19915>